Evaluation of laser speckle contrast imaging as an intrinsic method to monitor blood brain barrier integrity

Suzie Dufour,[1,2] Yaaseen Atchia,[1,2] Raanan Gad,[1,2] Dene Ringuette,[1,2] Iliya Sigal,[1,2] and Ofer Levi[1,2,*]

[1]*The Edward S. Rogers Sr. Department of Electrical and Computer Engineering, University of Toronto, 10 King's College Road, Toronto, ON M5S 3G4, Canada*
[2]*Institute of Biomaterials and Biomedical Engineering, University of Toronto, 164 College Street, Toronto, ON M5S 3G9, Canada*
*ofer.levi@utoronto.ca

Abstract: The integrity of the blood brain barrier (BBB) can contribute to the development of many brain disorders. We evaluate laser speckle contrast imaging (LSCI) as an intrinsic modality for monitoring BBB disruptions through simultaneous fluorescence and LSCI with vertical cavity surface emitting lasers (VCSELs). We demonstrated that drug-induced BBB opening was associated with a relative change of the arterial and venous blood velocities. Cross-sectional flow velocity ratio (veins/arteries) decreased significantly in rats treated with BBB-opening drugs, ≤0.81 of initial values.

© 2013 Optical Society of America

OCIS codes: (170.0110) Imaging systems; (170.3880) Medical and biological imaging; (140.2020) Diode lasers; (170.6480) Spectroscopy, speckle.

References and links

1. N. J. Abbott, A. A. K. Patabendige, D. E. M. Dolman, S. R. Yusof, and D. J. Begley, "Structure and function of the blood-brain barrier," Neurobiol. Dis. **37**(1), 13–25 (2010).
2. R. N. Kalaria, "The Blood-Brain Barrier and Cerebrovascular Pathology in Alzheimer's Disease," Ann. N. Y. Acad. Sci. **893**, 113–125 (1999).
3. M. B. Shlosberg, D. Kaufer, and A. Friedman, "Blood-brain barrier breakdown as a therapeutic target in traumatic brain injury," Nat. Rev. Neurol. **6**, 10 (2010).
4. O. Tomkins, I. Shelef, I. Kaizerman, A. Eliushin, Z. Afawi, A. Misk, M. Gidon, A. Cohen, D. Zumsteg, and A. Friedman, "Blood-brain barrier disruption in post-traumatic epilepsy," J. Neurol. Neurosurg. Psychiatry **79**(7), 774–777 (2008).
5. E. Seiffert, J. P. Dreier, S. Ivens, I. Bechmann, O. Tomkins, U. Heinemann, and A. Friedman, "Lasting Blood-Brain Barrier Disruption Induces Epileptic Focus in the Rat Somatosensory Cortex," J. Neurosci. **24**(36), 7829–7836 (2004).
6. W. H. Oldendorf, "Blood-Brain Barrier Permeability to Drugs," Annu. Rev. Pharmacol. **14**(1), 239–248 (1974).
7. W. M. Pardridge, "CNS Drug Design Based on Principles of Blood-Brain Barrier Transport," J. Neurochem. **70**(5), 1781–1792 (1998).
8. M. Kinoshita, N. McDannold, F. A. Jolesz, and K. Hynynen, "Noninvasive localized delivery of Herceptin to the mouse brain by MRI-guided focused ultrasound-induced blood-brain barrier disruption," Proc. Natl. Acad. Sci. U.S.A. **103**(31), 11719–11723 (2006).
9. S. I. Rapoport, "Osmotic Opening of the Blood-Brain Barrier: Principles, Mechanism, and Therapeutic Applications," Cell. Mol. Neurobiol. **20**(2), 217–230 (2000).
10. N. Sheikov, N. McDannold, N. Vykhodtseva, F. Jolesz, and K. Hynynen, "Cellular mechanisms of the blood-brain barrier opening induced by ultrasound in presence of microbubbles," Ultrasound Med. Biol. **30**(7), 979–989 (2004).
11. Q. Jiang, J. R. Ewing, G. L. Ding, L. Zhang, Z. G. Zhang, L. Li, P. Whitton, M. Lu, J. Hu, Q. J. Li, R. A. Knight, and M. Chopp, "Quantitative evaluation of BBB permeability after embolic stroke in rat using MRI," J. Cereb. Blood Flow Metab. **25**(5), 583–592 (2005).
12. P. S. Tofts and A. G. Kermode, "Measurement of the blood-brain barrier permeability and leakage space using dynamic MR imaging. 1. Fundamental concepts," Magn. Reson. Med. **17**(2), 357–367 (1991).

13. S. Taheri, E. Candelario-Jalil, E. Y. Estrada, and G. A. Rosenberg, "Spatiotemporal Correlations between Blood-Brain Barrier Permeability and Apparent Diffusion Coefficient in a Rat Model of Ischemic Stroke," PLoS ONE **4**(8), e6597 (2009).
14. M. Wintermark, J. Hom, J. Dankbaar, J. Bredno, and M. Olszewski, "Blood-brain barrier permeability: quantification with computed tomography and application in acute ischemic stroke," Dear Friends **53**, 3 (2009).
15. L. Ruiz-Valdepeñas, J. A. Martínez-Orgado, C. Benito, A. Millán, R. M. Tolón, and J. Romero, "Cannabidiol reduces lipopolysaccharide-induced vascular changes and inflammation in the mouse brain: an intravital microscopy study," J. Neuroinflammation **8**(1), 5 (2011).
16. D.-E. Kim, D. Schellingerhout, F. A. Jaffer, R. Weissleder, and C. H. Tung, "Near-infrared fluorescent imaging of cerebral thrombi and blood-brain barrier disruption in a mouse model of cerebral venous sinus thrombosis," J. Cereb. Blood Flow Metab. **25**(2), 226–233 (2005).
17. E. E. Cho, J. Drazic, M. Ganguly, B. Stefanovic, and K. Hynynen, "Two-photon fluorescence microscopy study of cerebrovascular dynamics in ultrasound-induced blood-brain barrier opening," J. Cereb. Blood Flow Metab. **31**(9), 1852–1862 (2011).
18. O. Prager, Y. Chassidim, C. Klein, H. Levi, I. Shelef, and A. Friedman, "Dynamic in vivo imaging of cerebral blood flow and blood-brain barrier permeability," Neuroimage **49**(1), 337–344 (2010).
19. D. A. Boas and A. K. Dunn, "Laser speckle contrast imaging in biomedical optics," J. Biomed. Opt. **15**(1), 011109 (2010).
20. A. Ponticorvo and A. K. Dunn, "How to build a Laser Speckle Contrast Imaging (LSCI) system to monitor blood flow," J. Vis. Exp. (45): (2010).
21. S. Yuan, A. Devor, D. A. Boas, and A. K. Dunn, "Determination of optimal exposure time for imaging of blood flow changes with laser speckle contrast imaging," Appl. Opt. **44**(10), 1823–1830 (2005).
22. P. Miao, H. Lu, Q. Liu, Y. Li, and S. Tong, "Laser speckle contrast imaging of cerebral blood flow in freely moving animals," J. Biomed. Opt. **16**(9), 090502 (2011).
23. Y. Atchia, H. Levy, S. Dufour, and O. Levi, "Rapid multiexposure in vivo brain imaging system using vertical cavity surface emitting lasers as a light source," Appl. Opt. **52**(7), C64–C71 (2013).
24. A. K. Dunn, H. Bolay, M. A. Moskowitz, and D. A. Boas, "Dynamic imaging of cerebral blood flow using laser speckle," J. Cereb. Blood Flow Metab. **21**(3), 195–201 (2001).
25. I. Sigal, Y. Atchia, R. Gad, A. M. Caravaca, D. Conkey, R. Piestun, and O. Levi, "Laser Speckle Contrast Imaging with Extended Depth of Field for Brain Imaging Applications," in *CLEO: Science and Innovations, Imaging & Microscopy I* (Optical Society of America, 2013), paper CTu2M.
26. A. K. Dunn, "Laser Speckle Contrast Imaging of Cerebral Blood Flow," Ann. Biomed. Eng. **40**(2), 367–377 (2012).
27. J. D. Briers, "Laser Doppler, speckle and related techniques for blood perfusion mapping and imaging," Physiol. Meas. **22**(4), R35–R66 (2001).
28. L. M. Richards, E. L. Towle, D. J. Fox, and A. K. Dunn, "Laser Speckle Imaging of Cerebral Blood Flow," in *Optical Methods and Instrumentation in Brain Imaging and Therapy* (Springer New York, 2013), pp. 117–136.
29. M. Kaiser, A. Yafi, M. Cinat, B. Choi, and A. J. Durkin, "Noninvasive assessment of burn wound severity using optical technology: a review of current and future modalities," Burns **37**(3), 377–386 (2011).
30. H. Levy, D. Ringuette, and O. Levi, "Rapid monitoring of cerebral ischemia dynamics using laser-based optical imaging of blood oxygenation and flow," Biomed. Opt. Express **3**(4), 777–791 (2012).
31. E. A. Munro, H. Levy, D. Ringuette, T. D. O'Sullivan, and O. Levi, "Multi-modality optical neural imaging using coherence control of VCSELs," Opt. Express **19**(11), 10747–10761 (2011).
32. M. B. Bouchard, B. R. Chen, S. A. Burgess, and E. M. Hillman, "Ultra-fast multispectral optical imaging of cortical oxygenation, blood flow, and intracellular calcium dynamics," Opt. Express **17**(18), 15670–15678 (2009).
33. J. Greenwood, J. Adu, A. J. Davey, N. J. Abbott, and M. W. Bradbury, "The effect of bile salts on the permeability and ultrastructure of the perfused, energy-depleted, rat blood-brain barrier," J. Cereb. Blood Flow Metab. **11**(4), 644–654 (1991).
34. H. Ichikawa and K. Itoh, "Blood-arachnoid barrier disruption in experimental rat meningitis detected using gadolinium-enhancement ratio imaging," Brain Res. **1390**, 142–149 (2011).
35. A. Saria and J. M. Lundberg, "Evans blue fluorescence: quantitative and morphological evaluation of vascular permeability in animal tissues," J. Neurosci. Methods **8**(1), 41–49 (1983).
36. A. Y. Shih, J. D. Driscoll, P. J. Drew, N. Nishimura, C. B. Schaffer, and D. Kleinfeld, "Two-photon microscopy as a tool to study blood flow and neurovascular coupling in the rodent brain," J. Cereb. Blood Flow Metab. **32**(7), 1277–1309 (2012).
37. H. P. Rani, T. W. Sheu, T. M. Chang, and P. C. Liang, "Numerical investigation of non-Newtonian microcirculatory blood flow in hepatic lobule," J. Biomech. **39**(3), 551–563 (2006).
38. L. Grinberg, V. Morozov, D. Fedosov, J. A. Insley, M. E. Papka, K. Kumaran, and G. E. Karniadakis, "A new computational paradigm in multiscale simulations: Application to brain blood flow," in *High Performance Computing, Networking, Storage and Analysis (SC), 2011 International Conference for*(IEEE, 2011), pp. 1–12.
39. S. Lorthois, F. Cassot, and F. Lauwers, "Simulation study of brain blood flow regulation by intra-cortical arterioles in an anatomically accurate large human vascular network. Part II: flow variations induced by global or localized modifications of arteriolar diameters," Neuroimage **54**(4), 2840–2853 (2011).

40. S. Lorthois, F. Cassot, and F. Lauwers, "Simulation study of brain blood flow regulation by intra-cortical arterioles in an anatomically accurate large human vascular network: Part I: methodology and baseline flow," Neuroimage **54**(2), 1031–1042 (2011).
41. R. Byron Bird and P. J. Carreau, "A nonlinear viscoelastic model for polymer solutions and melts—I," Chem. Eng. Sci. **23**(5), 427–434 (1968).
42. Y. I. Cho and K. R. Kensey, "Effects of the non-Newtonian viscosity of blood on flows in a diseased arterial vessel. Part 1: Steady flows," Biorheology **28**(3-4), 241–262 (1991).
43. A. Sequeira and J. Janela, "An overview of some mathematical models of blood rheology," in *A Portrait of State-of-the-Art Research at the Technical University of Lisbon*(Springer, 2007), pp. 65–87.
44. B. M. Johnston, P. R. Johnston, S. Corney, and D. Kilpatrick, "Non-Newtonian blood flow in human right coronary arteries: steady state simulations," J. Biomech. **37**(5), 709–720 (2004).
45. K. P. Ivanov, M. K. Kalinina, and Y. I. Levkovich, "Blood flow velocity in capillaries of brain and muscles and its physiological significance," Microvasc. Res. **22**(2), 143–155 (1981).
46. S. M. Stieger, C. F. Caskey, R. H. Adamson, S. Qin, F.-R. E. Curry, E. R. Wisner, and K. W. Ferrara, "Enhancement of vascular permeability with low-frequency contrast-enhanced ultrasound in the chorioallantoic membrane model," Radiology **243**(1), 112–121 (2007).
47. S. Lorthois and F. Lauwers, "Control of brain blood flow by capillaries: a simulation study in an anatomically accurate large human vascular network," Comput. Methods Biomech. Biomed. Engin. **15**(sup1), 66–68 (2012).
48. M. E. van Raaij, L. Lindvere, A. Dorr, J. He, B. Sahota, F. S. Foster, and B. Stefanovic, "Quantification of blood flow and volume in arterioles and venules of the rat cerebral cortex using functional micro-ultrasound," Neuroimage **63**(3), 1030–1037 (2012).
49. N. Nishimura, N. L. Rosidi, C. Iadecola, and C. B. Schaffer, "Limitations of collateral flow after occlusion of a single cortical penetrating arteriole," J. Cereb. Blood Flow Metab. **30**(12), 1914–1927 (2010).
50. J. Nguyen, N. Nishimura, R. N. Fetcho, C. Iadecola, and C. B. Schaffer, "Occlusion of cortical ascending venules causes blood flow decreases, reversals in flow direction, and vessel dilation in upstream capillaries," J. Cereb. Blood Flow Metab. **31**(11), 2243–2254 (2011).
51. M. B. Lawrence, L. V. McIntire, and S. G. Eskin, "Effect of flow on polymorphonuclear leukocyte/endothelial cell adhesion," Blood **70**(5), 1284–1290 (1987).
52. C. Skilbeck, S. M. Westwood, P. G. Walker, T. David, and G. B. Nash, "Population of the vessel wall by leukocytes binding to P-selectin in a model of disturbed arterial flow," Arterioscler. Thromb. Vasc. Biol. **21**(8), 1294–1300 (2001).
53. B. Arvin, L. F. Neville, F. C. Barone, and G. Z. Feuerstein, "The role of inflammation and cytokines in brain injury," Neurosci. Biobehav. Rev. **20**(3), 445–452 (1996).
54. K. Miyamoto, Y. Ogura, M. Hamada, H. Nishiwaki, N. Hiroshiba, and Y. Honda, "In vivo quantification of leukocyte behavior in the retina during endotoxin-induced uveitis," Invest. Ophthalmol. Vis. Sci. **37**(13), 2708–2715 (1996).
55. M. Bohatschek, A. Werner, and G. Raivich, "Systemic LPS injection leads to granulocyte influx into normal and injured brain: effects of ICAM-1 deficiency," Exp. Neurol. **172**(1), 137–152 (2001).
56. N. Parashurama, T. D. O'Sullivan, A. De La Zerda, P. El Kalassi, S. Cho, H. Liu, R. Teed, H. Levy, J. Rosenberg, Z. Cheng, O. Levi, J. S. Harris, and S. S. Gambhir, "Continuous sensing of tumor-targeted molecular probes with a vertical cavity surface emitting laser-based biosensor," J. Biomed. Opt. **17**(11), 117004 (2012).

1. Introduction

Exchanges between the blood and the central nervous system (CNS) are highly controlled by the blood brain barrier (BBB), essentially composed of endothelial tight junctions and astrocytic glial cell endfeet wrapped around small brain vessels [1]. A breakdown of the barrier's integrity can negatively affect normal brain behavior. For example, recent studies demonstrated that malfunction of BBB integrity is a key factor in many pathological brain states such as Alzheimer's disease and Post Traumatic Epilepsy (PTE) [2–5]. Conversely, lack of BBB permeability represents a challenge for drug delivery into the CNS [6, 7]. Consequently, many techniques are being developed to locally alter the barrier integrity and allow optimized local drug release into brain tissue [8–10]. It is thus often necessary to monitor the progression in BBB disruptions. MRI or CT scanners are used to monitor BBB integrity [11–14], as various MRI and CT parameters were proven to vary with BBB opening [11]. However, MRI and CT scanners are expensive to operate, are not optimized for prolonged measurement periods, and limit access to the subject during the recording period.

In preclinical studies on rodents, BBB permeability is often visualized and/or quantified using optical imaging methods and extrinsic fluorescent markers [15–17]. In fluorescent imaging, markers need to be injected within the vasculature, making these techniques inappropriate for continuous BBB permeability monitoring. Fluorescent dye can be re-

injected in multiple successive imaging sessions, but the typically long lifetime of the dye inside the vasculature and/or the tissue considerably increases the intervals at which imaging can be performed, leading to the reduction of the sampling rate.

As BBB opening is known to have an effect on cerebral blood flow [18], we studied the effect of BBB opening on blood flow velocity maps acquired with Laser Speckle Contrast Imaging (LSCI). LSCI is an intrinsic imaging technique that uses coherent light to measure wide-field relative flow velocity maps and offers high spatiotemporal resolution [19–21]. This technique has gained popularity in the past decade due to its simplicity, low cost, high spatio-temporal resolution, and its potential use in miniature, animal-mounted systems [22, 23]. The ability of the technique to measure flow velocities with high sensitivity has been confirmed by comparison to both Laser Doppler measurements [24], time of flight measurements in vivo [23], and in microfluidic systems in-vitro [25]. A number of review papers in the last few years outline the breadth of applications enabled by the technique in cortical blood flow imaging in healthy and damaged tissue [26–29].

Recently, we demonstrated that the coherence length of Vertical-Cavity Surface-Emitting Lasers (VCSELs) can be rapidly altered by applying different driving current modes (swept current and continuous current modes), thus making VCSELs an attractive illumination source for fast simultaneous measurements of blood flow and blood oxygenation via LSCI and Intrinsic Optical Signal Imaging (IOSI) modalities, respectively [30, 31].

Previous studies reported simultaneous wide-field fluorescence imaging and LSCI [20,32]. Here we show that a similar system can be replicated with low power VCSELs. VCSELs offer several advantages as compared to LEDs (size, sharp emission peak, low energy consumption, stability) and other laser sources (cost, size, rapid intensity, and coherence modulation), as further discussed in reference [31]. In this study, we acquired simultaneous relative velocity maps and vascular fluorescent maps during BBB opening and determined the effect of the opening on the relative velocity maps. Fluorescent dye imaging was used as a "gold standard" comparison technique to confirm BBB permeability changes and leakage. In addition, we simulated the effect of leaky vessel boundaries on the velocity maps to compare to our experimental observations. Our results show that the ratio between venous and arterial blood flow is significantly reduced in animals with compromised BBB, indicating that this parameter is a promising metric to assess BBB integrity. To our knowledge, this work represents the first demonstration that LSCI can be used as an intrinsic method for monitoring BBB integrity.

2. Methods

2.1 Evaluation of flow parameters

Figure 1 shows a schematic representation of vessels with both intact (Fig. 1(a)) and leaking (Fig. 1(b)) BBB. Based on the findings of Prager *et al.,* who used a method based on fluorescent labeling to monitor changes in blood flow dynamics [18], we hypothesized that local changes in flow can be observed in blood vessels located near leaking zones and that leakage at the capillary level (with or without red blood cell extravasation) would translate into a change in the vascular ouput/input balance, *i.e.* the ratio of the blood flowing in and out of the tissue. Figure 1(c) represents the transverse flow profile along the dotted line in Fig. 1(b), which defines the different parameters that were assessed in this study: (1) the maximum relative blood velocity (usually at the vessel center), (2) the diameter of the vessel (full width at half maximum of the velocity profile) and (3) the area under the transverse velocity profile (calculated as a spatial integration of the flow velocity values between the two sides of the vessel). The last parameter was measured because it comprises information on both (1) the relative blood velocity and (2) the vessel dilation (diameter change). The integrated velocity profile involves integrating the values of speckle contrast in the transverse direction. The local speckle contrast values effectively integrate speed over depth. Therefore, the transverse

velocity profile is an average integral of the speed in the two transverse directions along a vessel. Therefore, the integrated transverse velocity profile effectively shows the volume flux by multiplying speed by area.
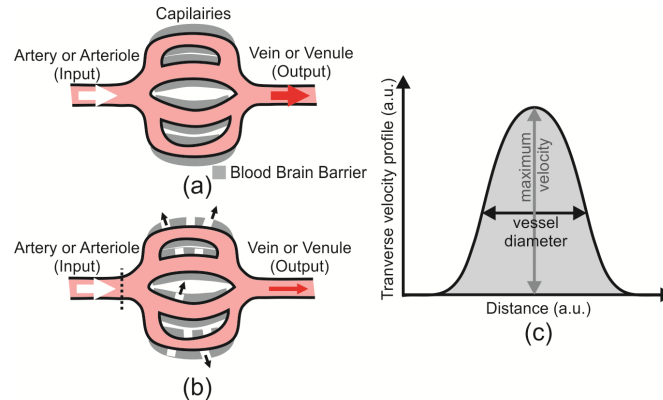

Fig. 1. (a) Hypothetical illustration of the blood flowing through an artery (or arteriole), capillaries and a vein (or venule), subsequently, in the condition of intact BBB. (b) Same representation for a compromised blood brain barrier, wherein the venous output (red arrow) is decreased. The input and output blood volumes are represented by white and red arrows, respectively. (c) Hypothetical transverse velocity profile along the dotted line (b) and definition of the different parameters measured and analyzed in this study. The maximal velocity amplitude is represented by the vertical arrow, the vessel diameter (full width at half maximum) is represented by the horizontal arrow, and the area under the transverse velocity profile is represented by the shaded area.

2.2 Animal preparation

The imaging studies were conducted on anesthetized (2-3% isoflurane) male Sprague Dawley rats (200-300g). All animal studies were performed in accordance with ethics protocols approved by the University of Toronto Animal Care Committee. After anesthesia induction, the animal was placed in a stereotaxic frame. A local analgesic (lidocaine cream, EMLA) was applied to all pressure points and tissues to be incised. The animal body temperature was maintained at 37.5°C using a thermal blanket (T/Pump, Gaymar Industries, Orchard Park, NY). Hind limb withdrawal reflex, heart and breathing rates were observed at regular intervals throughout the experiment to ensure that the animal remained at a surgical plane of anesthesia. A 5 mm diameter craniotomy was performed over the sensory cortex and the dura was carefully removed to expose the brain tissue to be imaged. As previously described [30, 31], the craniotomy was then surrounded with a petroleum gel track to form a well which was filled with 1-2% agarose gel. Subsequently, the gel track was covered with a coverslip to form a cranial window. Evans blue dye (Sigma, 1.5%, 1ml/kg) was injected via the tail vein. For local drug application, the well was filled with saline only. In five animals, a craniotomy was performed on both hemispheres, as described in section 3.2; a window was placed over the open skull area in one of the hemispheres while a saline bath (made from petroleum gel wall, surrounding the exposed skull area) was prepared over the second hemisphere. This configuration allowed for unilateral drug application by changing the solution in the bath. In two of these five animals, no fluorescent dye was injected to eliminate possible effect of dye injection on our results.

2.3 BBB opening

Lipopolysaccharide (LPS) or deoxycholic acid (DOC) were used to alter the blood brain barrier permeability [15, 33]. In a subset of experiments, we used tail vein injection of LPS (Sigma, 1 mg/kg) a drug known to induce a BBB opening [15]. Blood flow and fluorescence maps were acquired prior to, and two hours after, LPS injection, and were subsequently

compared to one another. We were also interested in observing the effect of a local BBB opening. Local application of LPS on the tissue, rather than intravenously, does not systematically induce a disruption of the BBB [34] and for this reason topical application of 2 mM DOC (dissolved in saline) was used for local BBB disruptions. In animals treated with DOC, relative blood flow and fluorescence maps were acquired prior to, and 30-40 minutes after, the application of the drug.

2.4 Optical imaging

A schematic representation of the imaging setup is shown in Fig. 2(a) Several VCSELs with different wavelengths (680, 795 and 850 nm) were incorporated into a small (~ 5 mm diameter) package (Vixar Inc., Plymouth, MN), to be used as an illumination source. The backscattered (or fluorescence) light was collected, collimated, and redirected onto a 14-bit EMCCD camera (Rolera EM-C[2], QImaging, Surrey, BC) with the help of two imaging lenses (Nikon, 28 mm f/2.8 and 50 mm f/1.4). This configuration led to 1.8X magnification, and images of 500 × 500 pixels (or 2 × 2mm) were acquired. To accommodate a fluorescence imaging configuration, two long-pass filters (NT54-753, Edmund Optics Inc., Barrington, NJ) were placed in between the two imaging lenses (where light is collimated) to sustain an efficient blocking of the 680 nm excitation light (OD >6), while allowing the emitted fluorescence light in wavelengths above 700 nm to pass through to the camera. A current source (Model 6221, Keithley Instruments Inc., Cleveland, OH) and a switch (Model 7001, Keithley Instruments Inc., Cleveland, OH) were used to power the VCSELs.
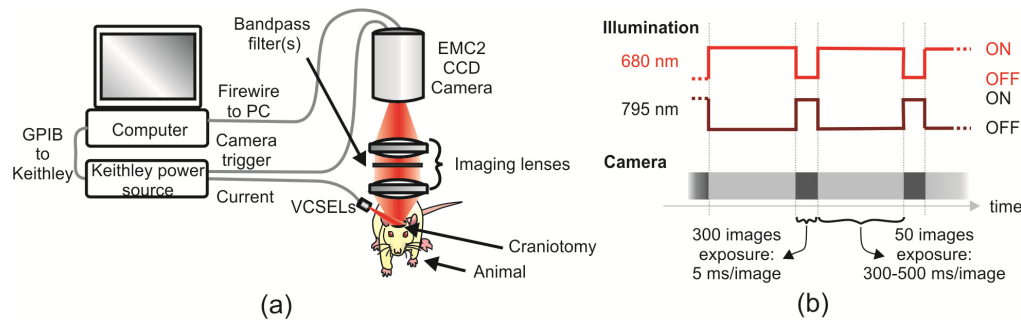

Fig. 2. Schematics of (a) the imaging experimental setup and (b) the illumination and image acquisition sequences.

For fluorescence images, Evans blue dye was excited by a 680 nm VCSEL source (swept driving current = 3-10 mA, optical power < 10 mW) and the camera integration time was set to 500 ms. The Evans blue dye was chosen because in its fluorescent form (when bound to albumin) it does not cross the intact BBB [35], the accumulation of fluorescence in the extravascular milieu was thus used to confirm BBB permeation. While a 680 nm wavelength is not centered at the peak of the Evans blue absorption spectra [35], it is well suited for fluorescence imaging since it creates sufficient fluorescence light that can be easily observed by our sensitive camera. Furthermore, the light in this excitation wavelength has reduced absorption by hemoglobin as compared to visible wavelengths.

For LSCI images, the tissue was illuminated by a 795 nm VCSEL (driving current = 1.2 mA, optical power < 1 mW) and the integration time was set to 5 ms to satisfy the long exposure time criteria suggested in [21]. Speckle contrast images were calculated from the raw reflection images obtained using a 5 × 5 pixel window around each pixel and averaged over 300 images to significantly reduce camera noise. 4-6 different depths were imaged to maintain all vessels in focus. In previous studies [30], a 680 nm VCSEL was chosen to illuminate the brain tissue in speckle imaging using the LSCI technique. The current choice of 795 nm as an illumination wavelength for speckle imaging allows a simultaneous recording of fluorescence and speckle maps. This is done through a coded sequence of 50

fluorescence images acquired at high exposure times (300 - 500 ms) followed by 300 short-exposure (5 ms) speckle contrast images using the 795 nm VCSEL (Fig. 2(b)). The use of a single VCSEL package for both wavelengths of illumination retains the advantages of a VCSEL as a fast, low cost, and miniature light source for optical brain imaging.

The temporal averaging performed in such manner enables extraction of robust flow values that are insensitive to transient and inhomogeneity of flow and scatter density, while retaining spatial (~10μm) and temporal (1.5 seconds per data point, repetition period of 16.5 seconds) resolution that is sufficiently high for the measurement performed.

2.5 Evaluation of BBB leakage on LSCI maps

The study was performed in two phases. The goal of the first phase was to determine the appropriate flow parameter to be used as a metric of BBB integrity compromise, while the goal of the second phase was to evaluate the efficacy of the metric to observe the temporal evolution of BBB permeability. The first phase of this study was performed on 15 rats separated into three distinct groups; a control group (n = 5), a second group treated with LPS (n = 4), and a third treated with DOC (n = 6). In animals treated with LPS, the BBB opening is global and all vessels are expected to be included in a treated region; we thus considered any vessel as being in the Region of Interest (ROI). However, in animals treated with DOC (local BBB opening) we only considered the arteries and the veins arising from the treated region. While the specific veins in the ROI may not always be fully related to the arteries that we observed in that ROI, we note that any arteries and veins that are diving vertically into an affected ROI region will have their relative velocities disturbed upon BBB opening (see for example Fig. 1 in [36]). For all groups (control, DOC and LPS) we evaluated blood velocity values and velocity profiles in different vessels. For the control group, 14 arteries (with diameters ranging from 60 to 300 μm) and 20 veins (diameters ranging from 60 to 260 μm) in five rats were analyzed. For the DOC group, the hemodynamic properties were evaluated for 21 arteries (diameters ranging from 45 to 230 μm) and 26 veins (diameters ranging from 85 to 400 μm) in six rats. For the LPS group, the same parameters were measured in 11 arteries (diameters ranging from 70 to 170 μm) and 15 veins (diameters ranging from 145 to 400 μm) in four rats. Only animals that showed no initial perioperative damage (brain swelling and dye leakage prior to drug application, noted in two animals) were used in this study.

In each animal, the hemodynamic changes of 3-5 veins and 3-5 arteries in the focal plane of the region of interest (ROI) were analyzed. These numbers were chosen according to the number of arteries and veins diving in the imaged ROI. Arteries and veins were identified visually by their morphology, diameter, branching pattern, and flow direction, as well as by their reflectance under green and red LED illumination, which differ due to their different concentrations of oxy- and deoxy-hemoglobin. The transverse flow profile of each vessel was traced and the three parameters defined in Fig. 1(c) were measured. In order to compare the effects in the different vessels, all measurements were normalized to their respective initial values. We then compared the changes observed in veins and arteries and calculated the relative changes in the output/input ratio, *i.e.* the relative changes observed in veins divided by the relative changes observed in arteries.

For the second phase of this study (n = 3 rats), LSCI-derived relative velocity maps and fluorescence maps were continuously acquired. Both hemispheres were simultaneously imaged. The temporal behavior of both arterial and venous velocities was analyzed for the drug-treated (DOC) and the control hemispheres, and compared to the rate of fluorescent dye leakage to evaluate the temporal progression of BBB opening on a given brain hemisphere.

2.6 Flow simulations

In support of our experimental flow velocity studies in a rat brain, we simulated blood flow velocities in a topology that resembles a section of the brain with leading arteries and collecting veins. We modeled an artery-like vessel (80 μm diameter) as an "inlet" branching

into different arterioles, capillaries and venules (5-20 μm diameter) which then reconnected in a vein-like compartment (200 μm diameter). The simulated geometry has a total length of 2000 μm (Fig. 3). Geometries and dimensions were chosen according to previous imaging studies [36].
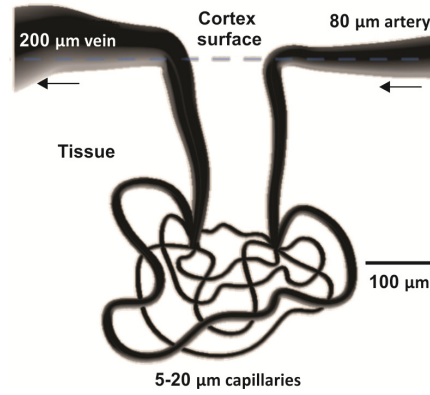

Fig. 3. Simulated geometry of an 80 μm artery diving into the cortex tissue, branching into 5-20μm capillaries, and uniting into a surfacing 200 μm vein.

To provide better insight into the flow dynamics we included limited redundancy of the vascular network at the capillary level, even though accurate velocities and pressures for microcirculatory networks were demonstrated in simpler models [37]. We considered the blood as a non-Newtonian fluid (NNF) where the viscosity, η, is dependent on shear rate or shear rate history. This model captures the effects of the individual red blood cells on the flow through the properties of the fluid, as opposed to explicitly simulating them as a separate portion of the blood stream, thus enabling the observation of the general flow behavior. While more complex models consider the flow of red blood cells, they are, nevertheless, based on numerous assumptions and require extensive computational resources [38–40].

The relation between the shear stress and the shear rate for NNF is non-linear, and can be time-dependent. The viscosity of blood is time-dependent and tends to decrease with increased stress. The Carreau power-law fluid model is a common model used to describe the viscosity of blood [41–43], and is depicted by the equation:

$$\eta(\dot{\gamma}) = \eta_\infty + (\eta_0 - \eta_\infty)\left[1 + (\lambda\dot{\gamma})^2\right]^{\frac{n-1}{2}} \qquad (1)$$

where η_∞ is the viscosity at infinite shear rate [Pa × s], η_0 is the viscosity at zero shear rate [Pa × s], λ is the relaxation time [s], n is the power index, and $\dot{\gamma} = \partial\gamma/\partial t$ [1/s], is the shear rate.

At low shear rate ($\dot{\gamma} \ll \lambda^{-1}$) Carreau fluid behaves as a Newtonian fluid, and at high shear rate ($\dot{\gamma} \gg \lambda^{-1}$) as a power-law fluid. Thus, in large- and medium-sized vessels, blood behaves as a homogeneous incompressible ($\nabla \cdot \vec{u} = 0$) Newtonian fluid, with flow behavior described by the time-dependent Navier–Stokes equation:

$$\rho\frac{\partial\vec{u}}{\partial t} + \rho(\vec{u}\cdot\nabla)\vec{u} = \nabla\cdot\underline{\sigma} + \vec{f} \qquad (2)$$

Here u denotes the flow velocity vector, ρ is the constant fluid density, and σ is the stress tensor. The flow dynamics in small capillaries is described using the time-dependent viscosity given by the Carreau model (Eq. (1)), where $\sigma = -p\underline{I} + 2\eta(\dot{\gamma})\underline{D}$ (p is the isotropic pressure,

I is the identity tensor, and D is the rate of deformation tensor), and f are the external body forces per unit volume (e.g. gravity).

The COMSOL Multiphysics finite element method (FEM) suite was used to study the changes in the blood flow dynamics due to leakage in the capillaries connecting arteries and veins in the presence of a localized leaky boundary. We solved the time-dependent Navier–Stokes equation (Eq. (2)) by introducing the time-dependant viscosity predicted by the Carreau model (Eq. (1)) into the stress tensor σ. We considered a simplified model where the inflow was set as a constant ($u_{in} = 10$ [mm/s]) and the outflow had a zero-pressure boundary condition. The flow is considered laminar while the blood is treated as an incompressible NNF with density $\rho = 1060$ kg/m^3 and the viscosity of which is obtained from the Carreau model. Following Eq. (1), the parameters for the time-dependent viscosity are given in ref [44] and ref [42], where $\eta_\infty = 0.00345$ Pa × s, $\eta_0 = 0.056$ Pa × s, $\lambda = 3.13$ s and $n = 0.3568$. Note that the blood flow velocity, u, in healthy brain capillaries varies between 5 mm/s for large (5-10 μm diameter) and < 1 mm/s for small (< 5 μm diameter) capillaries [30, 45].

3. Results

3.1 Experimental effect of BBB opening on the hemodynamics of veins and arteries

Simultaneous recordings of the relative velocity map, using the LSCI technique, and of the fluorescence map from a fluorescent dye marker, Evans blue, were used to evaluate the permeability of the BBB in response to application of drugs. Following drug application, the observation of extravascular fluorescence from the dye that was accumulated over time outside the vessels was used to confirm the presence of a leaky BBB (see Figs. 4(a), 5(a) and Fig. 9(a) in the Appendix). Figure 4(a) shows an example of fluorescence and relative velocity maps before (labeled "initial" in the figure) and after topical application of DOC, targeting a local opening of the BBB (labeled "DOC" in the figure), respectively. As shown in the fluorescence images (Fig. 4(a), bottom two panels), DOC induced a large permeability change and resulted in dye leakage from the vessels. Therefore, the vasculature that was clearly visible in the "initial" image is hardly visible in the final fluorescence image (even in the best focus plane). Correspondingly, this large permeability change has resulted in visible changes in the flow velocity map (Fig. 4(a) top panels). The vasculature, for the most part, remains visible in the LSCI-derived relative blood flow map. There is a noticeable arterial vasodilatation accompanied by a net velocity reduction in many veins, as can be better seen by plotting the difference in flow velocities from their initial values after DOC application (Fig. 4(b)). Examples of relative flow profile for an artery and for a vein (both locations are marked with a thick black line in Fig. 4(a)) overlaid by a fit to a parabolic flow velocity profile are shown in Fig. 4(c), in the upper and lower panels, respectively.

Another example of the effect of DOC application, where the permeability changes in the brain vessels for an individual rat were more subtle, is shown in Fig. 9. Note that in this case, fluorescence accumulation in the extravascular medium was observed only in discrete zones (see arrow in Fig. 9, bottom right panel), and relative flow profiles for an artery and for a vein near the fluorescent dye accumulation region (black lines in Fig. 9(a)) show smaller changes as well.
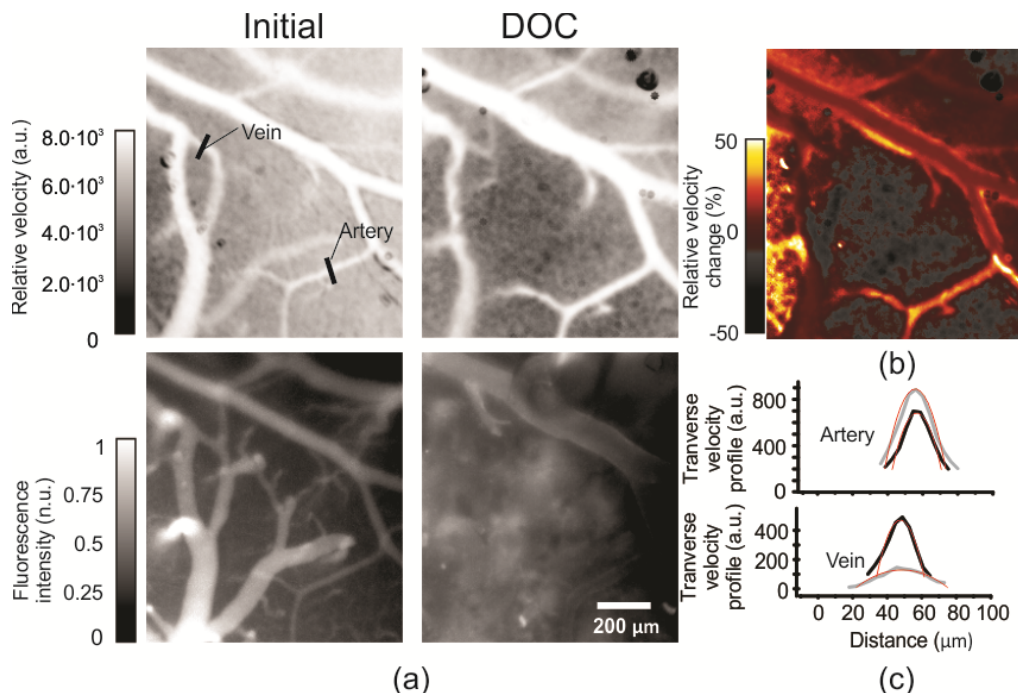
Fig. 4. DOC-induced BBB opening signature in the blood velocity map. (a) Fluorescence intensity and blood relative velocity maps before and after DOC application. (b) Relative changes of flow velocity after DOC application. (c) Relative blood velocity profiles were traced for an artery (upper) and a vein (lower) before and after DOC application. The DOC fluorescence and relative velocity images were recorded 30 minutes after the drug application. Initial profiles are traced in black and the final ones are traced in grey. Locations of the profiles shown in (c) are highlighted in panel (a) by the black bars.

Figure 5 shows a similar effect for the LPS-induced BBB permeability changes. Simultaneous recordings of the relative velocity map, and of the fluorescence map from the same fluorescent dye, Evans blue, were used to evaluate global changes in the permeability of the BBB in response to a tail vein injection of LPS. Figure 5(a) shows an example of the fluorescence and relative velocity maps before (labeled "initial" in the figure) and after tail vein injection of LPS, targeting a global opening of the BBB (labeled "LPS" in the figure), respectively. The action of the LPS drug was slower than that of the DOC drug. Consequently, the final maps were obtained 120 minutes after LPS injection. A clear observation of extravascular fluorescence from the dye due to opening of the BBB (Fig. 5(a), bottom two panels) was accompanied with a reduction of the relative flow velocity (Fig. 5(a), top two panels). There was no noticeable arterial vasodilatation. The reduction in net velocity in the arteries was accompanied by a larger net velocity reduction in many veins. The difference in flow velocities from their initial values is shown in Fig. 5(b). This difference can be seen in an example of the relative flow profile for an artery and for a vein (both marked with a thick black line in Fig. 5(a)) overlaid by a fit to a parabolic flow velocity profile in Fig. 5(c).
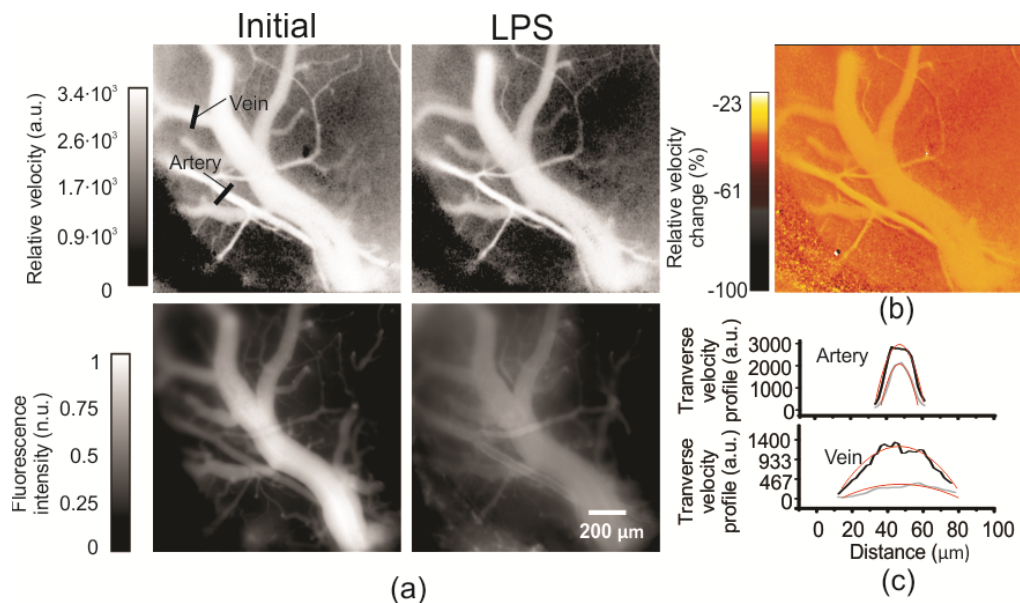
Fig. 5. LPS-induced BBB opening signature in the blood velocity map. (a) Fluorescence intensity and blood relative velocity maps before and after LPS application. (b) Relative changes of flow velocity after LPS application. (c) Relative blood velocity profiles were traced for an artery (upper) and a vein (lower) before and after LPS application. The LPS fluorescence and relative velocity images were recorded 2 hours after the drug application because LPS effect was slower. Initial profiles are traced in black and the final ones are traced in grey. Locations of the profiles shown in (c) are highlighted in panel (a) by the black bars.

Our experimental data, shown in Figs. 4 and 5, suggests that BBB opening has a different effect on flow speeds in veins and arteries. There are several physiological factors that may affect the local individual flow velocities (anesthesia state and duration, body temperature, compensation process for the lost intravascular fluid, etc.), which will be discussed in section 4. In order to separate these possible effects and other factors causing spontaneous hemodynamic changes that are not related to BBB opening, we evaluate a "macroscopic" variable influenced by the drug-induced permeability changes, namely *the ratio of the output velocities and input velocities*.

The output/input ratio of the relative velocity values was evaluated for the three parameters defined in Fig. 1(c), namely (1) the maximum flow velocity value (amplitude), (2) vessel diameter, and (3) integrated transverse profile. The histogram presented in Fig. 6 shows a calculation of the output/input ratio for each parameter measured in the three distinct animal populations (control, DOC-treated, LPS-treated). The values of the integrated transverse profile output/input ratios (parameter 3) normalized according to initial values are 1.03 ± 0.04, 0.78 ± 0.06 and 0.70 ± 0.07 for the control, DOC-treated and LPS-treated animal populations respectively (data shown as mean $\pm$ SE). Note that while there seems to be a slight reduction in the vessel diameter ratios (2) in treated animals, no statistically significant changes in this parameter were observed. The integrated transverse profile (3) showed a statistically significant reduction in the output/input ratio after DOC (two tailed t-test, p = 0.01) and LPS treatment (two tailed t-test, p = 0.02) when compared to the initial values and when compared to the control group (p = 0.04 and 0.03 respectively).
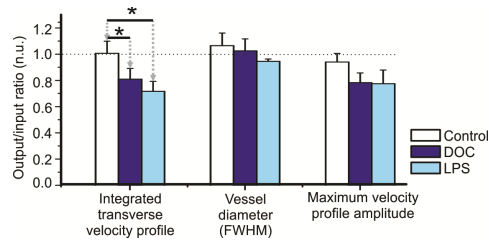
Fig. 6. BBB opening and permeability change effects on the vascular output/input ratio. To compare the veins and arteries hemodynamics before and after drug-induced BBB disruption, three parameters were measured in veins and arteries: the vessel diameter, the maximum relative flow and the profile area. These parameters were normalized to initial values and used to calculate the output/input ratios, *i.e.* the relative change in veins divided by the relative change in arteries for each measured parameters. Output/Input ratios for different parameters: the vessel diameter (width at half maximum of the velocity profile), the maximum relative velocity (the maximum of the velocity profile) and the transverse profile area (the area under the relative velocity profile curve) are shown in control animals (white, n = 5 rats (14 arteries and 20 veins)), in animals treated with DOC (dark blue, n = 6 rats (21 arteries and 26 veins)) and in animal treated with LPS (pale blue, n = 4 rats (11 arteries and 15 veins)). For each animal, the ratio was normalized according to the initial values (* = p < 0.05).

3.2 Continuous monitoring

Temporal evaluation of the effect of the DOC drug, before and after application (Fig. 4), showed that while individual arteries and veins may be susceptible to velocity fluctuations during the induced BBB permeability changes. The calculated ratio of venous and arterial blood velocity aggregated over several vessels in the ROI was significantly reduced in treated animals and can be used as a metric to assess BBB integrity. Simultaneous observation of fluorescence and speckle-derived relative velocity maps in two regions of the brain, while only one of them was treated with DOC, validates the assertion that the "control" side is minimally affected by the permeability changes, and that the velocity maps clearly differentiate between the regions where the BBB was altered, and the regions where the BBB was intact in the same animal. As described in the methods section, two cranial windows were prepared and DOC was applied in only one of the cranial windows, allowing the untreated hemisphere to serve as a reference (see Fig. 7(a)). Figure 7(b) shows the fluorescence (top two panels) and relative velocity (bottom two panels) maps after DOC application. A clear accumulation of dye outside the vessels was shown in fluorescence image (top right) for the treated hemisphere. Overlaid on the relative velocity image for the treated hemisphere (bottom right) is a marking for regions inside a vein, inside an artery, and in the extravascular tissue where the temporal evolution of the relative flow velocity is traced, as shown in Fig. 7(c). While the temporal curves for all tissue compartments (vein, artery and tissue) show a monotonic slow reduction in the blood velocity of ~10% over an hour, the drug-treated hemisphere (bold lines, Fig. 7(c)) clearly shows an effect in permeability change that results in relative velocity changes. In this animal, the observed velocity in the drug-treated hemisphere has increased in all of these tissue compartments. However, the increase was stronger for the artery, leading to an effective reduction in the output/input ratio for these individual vessels. Moreover, our analysis shows that the output/input integrated transverse profile ratio, calculated for several veins and several arteries in the ROI, was significantly reduced in the treated area (Fig. 7(d), thick bold time traces), as compared with the untreated "control" hemisphere, in agreement with the findings reported in Fig. 6. Taken over (n = 5 rats) the output/input ratio (integrated transverse velocity profile ratio) was reduced after DOC application to the treated hemisphere (Fig. 7(d), bar graph). This reduction in flow velocity ratio was associated with an increase of the extravascular tissue fluorescence intensity due to dye accumulation (Fig. 7(e)), indicating that it is related to permeability changes and opening of the BBB.
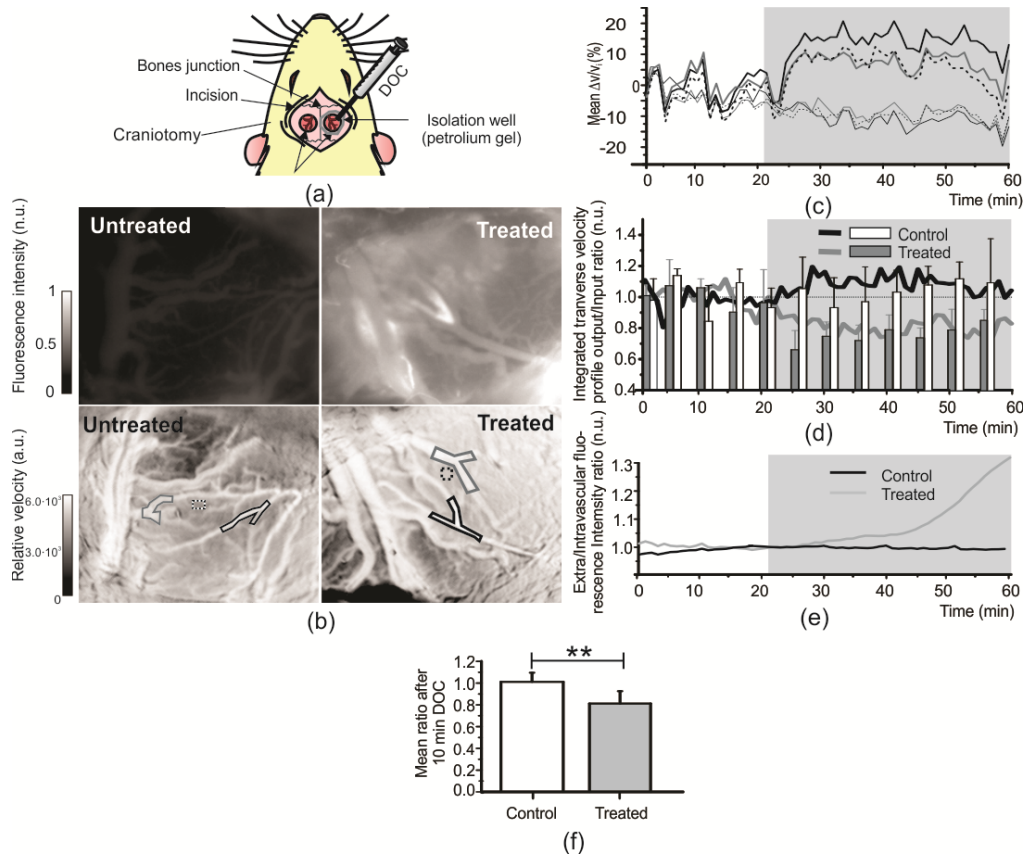
Fig. 7. Simultaneous observation of fluorescence and blood flow velocity maps in treated and untreated hemispheres. (a) Schematic representation of the surgical procedures. (b) Fluorescence (top) and relative velocity (bottom) maps for untreated "control" hemisphere (left two panels) and treated hemisphere (right two panels) as they appear 60 minutes after DOC application on the right treated hemisphere. (c) Temporal evolution of the relative flow velocity in different tissue compartments for the treated (bold lines) and untreated hemispheres. Artery (black), vein (grey) and extravascular tissue (dotted lines) are presented. The regions over which the relative velocities were averaged are highlighted in panel b. (d) Time course of the normalized integrated transverse output/input profile ratio (bar graph, data shown as mean ± SE) and for the ratio calculated from the vessels shown in (b)-(c) (thick bold time traces). (e) Extravascular fluorescence accumulation for a treated and control regions. Note that in panels (c)-(e), the DOC application duration is represented by a grey zone. (f) Mean output/input ratio 10 minutes after DOC application (n = 5 rats, ** = p < 0.01, data shown as mean ± SD).

The mean output/input ratio (integrated transverse velocity profile ratio) was reduced to 0.81 ± 0.11 after 10 minutes of DOC application (Fig. 7(f)). This reduction is significantly different than the ratio observed in the untreated "control" hemisphere, 1.01 ± 0.08 (n = 5 rats, p = 0.002). Dye was injected at the beginning of the experiment, 20 minutes before DOC application, to better resolve the effects due to dye injection and DOC application. However, since the dye injection caused an increase in blood volume that could affect blood flow and even compromise the BBB integrity, two experiments were performed without dye injections and fluorescent imaging. Even without dye injection, DOC application led to a reduction of the output/input ratio (Fig. 10 in the Appendix). The time dynamics of the response was similar to those observed with the dye present in the blood stream.

3.3 Flow simulation of leaky vessels

In parallel to our experimental studies, we sought to evaluate if a change in BBB permeability can be observed in velocity changes in our model. In order to first validate the model, we compared simulated and measured flow velocities without leaking condition in a flow map shown in Fig. 11 in the Appendix. The absolute velocities were measured using the time of flight technique described in [30]. The simulated velocity values match the measured velocities with an average absolute variance of $12.0 \pm 9.0\%$ (Table 1 in the Appendix). Both simulated and measured values are in good agreement with our previous studies and literature [30, 36].
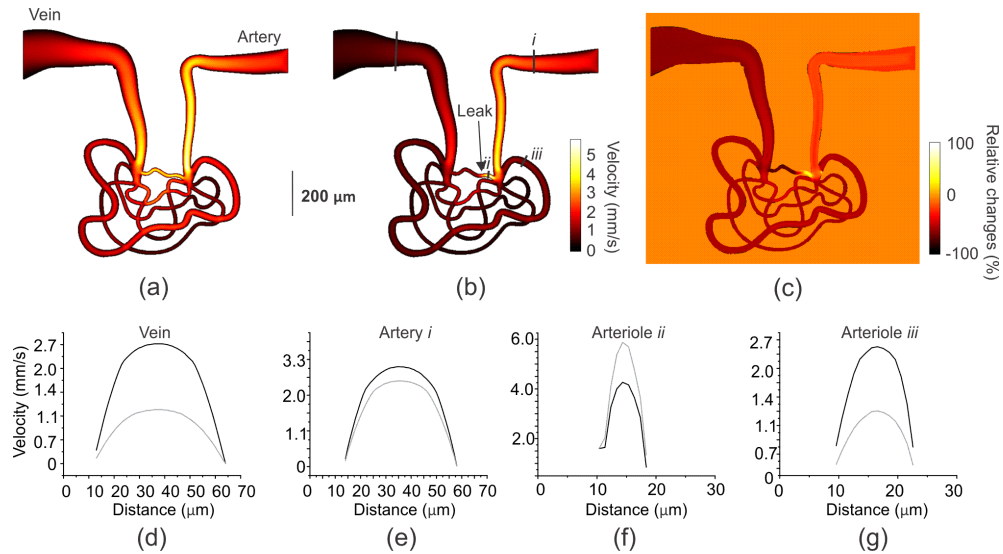

Fig. 8. Simulated effects of a localized leakage on velocity maps. a-b) Velocity maps without (a) and with (b) leaky boundary conditions. The arrow in (b) shows the location of the leaking zone. (c) Velocity changes calculated as $100 \cdot (v_f - v_i)/ v_i$, where v_f is the final velocity (with leak) and v_i stands for the initial velocity (no leak). (d) Initial (black curve) and final (grey curve) transverse velocity profile of the simulated vein. (e-g) Initial and final transverse velocity profiles of different simulated arteries or arterioles. Lines along which the profiles were taken (corresponding to locations i, ii, iii) are marked in panel (b).

Figure 8(a)-8(b) shows the simulated schematic of a vasculature topology before and after applying leaky boundary conditions. When comparing the simulated relative velocity maps in intact conditions (Fig. 8(a)) to a case where localized leaky boundaries were added to a capillary (see arrow in Fig. 8(b)), we observed changes in the relative flow velocities. These changes become clearly visible in the velocity changes map (Fig. 8(c)), calculated as $(v_f - v_i)/v_i$, where v_f is the final velocity (with leak) and v_i stands for the initial velocity (no leak). According to our simulations, a leakage affects velocities upstream and downstream (see Fig. 8(d)-8(g)) of the capillary bed). Note that in the present case, only one leaking zone was simulated (20 µm length leaking zone and the leaking velocity at the boundary varies from 0 to 0.2 mm/s within 2 s and follows $u_{leak} = u_0[1 + \tanh(t-t_0)]$ [mm/s]) [46]. The leak results in complex velocity changes and depending on the location of the leak the effect on the velocity measured in one artery (or one arteriole) may differ (see Fig. 8(e)-8(g)). However, there seems to be a constant drop in the blood output/input velocity ratio when comparing the velocity in the superficial vein and the arteries. Different leaking conditions (opening sizes, flow velocities, and locations of opening in the network) repeat the general trend, showing a decrease of the vein-artery flow velocity ratio. As such, in these scaled-down simulations we chose to scale down the amount of leakage proportionally.

Similarly, we have evaluated the effect of a partial occlusion on cerebral blood flow. The leaking zone was replaced by a vessel diameter reduction by a factor 2 over a 20 μm length. Occlusion led to a rerouting of blood in the vessel network but no change in the output/input velocity ratio is seen (see Fig. 12 in the Appendix).

4. Discussion

In this study we used the intrinsic LSCI technique to observe changes in flow velocity and related parameters, such as the flow output/input ratio, accompanying drug-induced BBB opening.

A comparison of the hemodynamic response for arteries and veins penetrating a given region in the cortex allows us to infer on the microvasculature state in deeper cortical layers. Our most important observation is the different manner that the arterial and venous velocities changed (see experimental example in Figs. 4(c) and 5(c), Fig. 9(c) and results derived from simulations in Fig. 8(d)-8(g)). Notably, observing the superficial arterial and venous flow velocities informs us on the state of the underlying vessel network, including the BBB integrity, over time. Initially we expected to observe a decrease in venous velocity following BBB disruption due to capillary leakage, but this predicted reduction of the venous flow was observed in only 45% of the veins in the ROI and, interestingly, an increase in arterial flow velocities was observed in 64% of the arteries in the ROI, across all animals in our study. This suggests a local physiological compensation mechanism for the losses in fluid volume to the extravascular tissue space. This compensation could be due to signaling implicating nearby cells causing an arterial vasodilatation upstream.

Several factors can influence the local flow dynamics for individual vessels, including the state and duration of the anesthesia. No statistically significant changes in raw velocity values in individual veins and arteries were observed; we thus used the ratio of venous to arterial integrated velocity profile as a metric for compromised BBB. This self-referencing of the measurements reduced the effect of other physiological factors involved in regulation of blood flow in the brain, as well as the effects of possible changes in absorption and scattering properties of the tissue following drug application. Applying a drug to disrupt the BBB significantly decreased this ratio, indicating a permeability change in the BBB. Indeed, this ratio was reduced by $22 \pm 6\%$ (final ratio of 0.78 ± 0.06) after DOC application and $30 \pm 7\%$ (final ratio of 0.70 ± 0.07) after LPS injection, which is statistically meaningful (see histogram in Fig. 6). The reduction of the vasculature output/input ratio after LPS or DOC treatment is believed to be due to a leakage at the capillary bed and superficial vessels. This leakage was confirmed by observing the accumulation of extravascular fluorescent dye, as shown in Figs. 4(a) and 5(a). Furthermore, the same output/input ratio was measured in rats where only one hemisphere was treated with DOC. The output/input ratio calculated 10 minutes after drug application was significantly smaller than the one calculated from the control hemisphere (0.81 ± 0.11 and 1.01 ± 0.08 respectively), as shown in Fig. 7(f). This is consistent with the values reported in Fig. 6. A reduction of the same ratio was also observed in animals where no fluorescent dye was used (Fig. 10).

Our simulations provide insight as to the leakage dynamics due to focal BBB opening. Simulated velocity maps have confirmed that the vein/artery velocity ratio decreases due to leakage from the blood vessels. The simulation results (Fig. 8) are in good agreement with the experimental observations. Although these simulations represent a simplified version of the realistic brain vascular network compared to more extensive computational flow model [38, 39, 47] (limited redundancy, use of a homogenous fluid without simulated blood cells), the general behavior depicted by the model was in agreement with values reported using the more complex models.

A possible limitation of the LSCI-based technique that we currently see is that each area under study must contains a few diving veins and arteries to ensure statistically significant results, thereby requiring a large field of view and potentially limiting the spatial resolution of

this technique. A potential solution is to measure the velocity in smaller arterioles, venules and capillaries located in deeper cortical layers using a higher magnification optical imaging system. Another limitation of using LSCI is the depth resolution provided by the technique, since the contrast ratios calculated for each pixel are affected by moving scattering elements above and below the vessel of interest. To limit the effect of underlying vessels more than one vessel was analyzed, and vessel cross sections were also chosen to avoid non-quadratic distribution when possible. The balance between arterial and venous flow could also potentially be measured with other techniques such as functional micro-ultrasound, recently reported by van Raaij and colleagues [48]. Their method quantifies blood flow and volume in arterioles and venules. Nevertheless, LSCI remains an advantageous solution when cost, portability, and simplicity are considered.

It is important to keep in mind that using LPS and DOC to instigate the BBB opening triggers a complex inflammatory response, leading to osmotic exchanges, recruitment of cells such as leukocytes, and thrombosis, which can also affect flow values. For example, it was demonstrated that thrombosis caused a rerouting [18, 49, 50]; the observed changes were similar for superficial veins and arteries. A decrease in both arterial and venous flow speeds was observed near the thrombosis site and a compensating increase was observed in peripheral regions [18]. These results are consistent with our occlusion simulation (Fig. 12), which predicts homogenous changes across arteries and veins and no change in the output/input ratio. It is challenging to completely separate BBB opening from the aforementioned effects since they are interconnected. Indeed, it was reported that flow is an important factor in leukocytes adhesion [51, 52]. Nevertheless, the inflammatory response and the recruitment of immune cells depend on several processes including the expression of binding proteins occurring minutes/hours after the insults [53]. Overall, the following four factors suggest that changes observed in the first minutes following drug application are caused by leakage: 1) the reported and simulated effect of thrombosis on cerebral blood flow is uniform over veins and arteries, 2) the time required for cell rolling and attachment to the vessel wall (reported to be several tens of minutes, even hours [54, 55]), 3) similar flow changes observed in previous studies with a different modality [18], and 4) good agreement between the temporal behavior of the fluorescent dye accumulation outside the vessel and the observed changes in venous/arterial flow ratio. Nevertheless, the contribution of occlusions, osmotic changes, and other contributors to the flow changes remain to be better investigated.

We emphasize that the sensitivity of the LSCI technique well exceeds the threshold required to observe the ~20% changes in arterial-to-venous flow ratio we report on. Calibration against absolute velocities *in vivo* [23] and *in vitro* [25] show the ability to discern flow speed changes of <5% reliably. The expected profile shape of the vessels is parabolic; such profile is observed in the centre of the blood vessels using the LSCI technique. We note that experimentally observed deviations from the parabolic shape near vessel edges are due to the convolution of the raw speckle images with the 5 x 5-pixel-wide filter, leading to blurring of the vessel edges due to the contribution of the static scatterers in the nearby tissue.

The sampling rate of fluorescence imaging methods to monitor the state of the BBB is limited by the dye's lifetime within the vasculature. For example, our recent studies using Cy5.5 based molecular markers have shown fast dye accumulation dynamics (within the first ~20 minutes) and long dye retention dynamics (typically for hours inside the body) [56]. Furthermore, our data indicates (Fig. 7(c), 7(d), 7(e)) that the flow response to barrier permeability change is visible several minutes prior to an appreciable change in the fluorescence signal, rendering our proposed technique better suited to studies where precise permeability change dynamics are of interest. Our proposed technique can also present an alternative to such modalities as MRI and CT, which require expensive instrumentation and allowing little access to the subject, and are drawbacks in experiments where a large number of animals need to be studied or in experiments where additional drugs need to be administered into the animal following BBB permeability change.

5. Conclusion

In this work we demonstrated that the ratio of arterial and venous flow profiles measured by wide-field LSCI are affected by LPS and DOC application and that LSCI is a potential low-cost, label-free technique to monitor the BBB integrity in a live rodent brain, with a possibility for application in long (hours to days) imaging sessions. Using a simultaneous measurement of fluorescence intensity of a dye leaking from vessels and relative velocity changes, we observed that arteries and veins respond differently to a drug-induced blood brain barrier opening. We proposed to measure the ratio between arterial and venous blood velocities as a metric to track the BBB disruption dynamics. Our numerical simulations in the simplified blood network model agree well with our experimental findings. The integrated transverse velocity profile ratio was shown to be the most promising metric for assessing the changes associated with drug-induced BBB opening. Along with further understanding of the hemodynamic and the physiological changes associated with localized BBB leaky boundaries, the technique proposed in this paper will help narrow the parameters to be measured to assess BBB integrity, and help develop screening protocols in monitoring brain diseases such as Alzheimer's disease and post-traumatic epilepsy.

Appendix

In this Appendix we include supplementary information, supporting our studies on the evaluation of LSCI as a technique for monitoring the BBB integrity in a live rodent brain. An example of the effect of DOC application, where the permeability changes in the brain vessels for an individual rat were subtle, is shown in Fig. 9. The time course of the normalized integrated transverse output/input profile ratio without dye injections is shown in Fig. 10. Table 1 show the measured and simulated velocity values for the vessel morphology maps marked in Fig. 11. Fig. 12 shows the simulated effects of a localized clog on a velocity map.
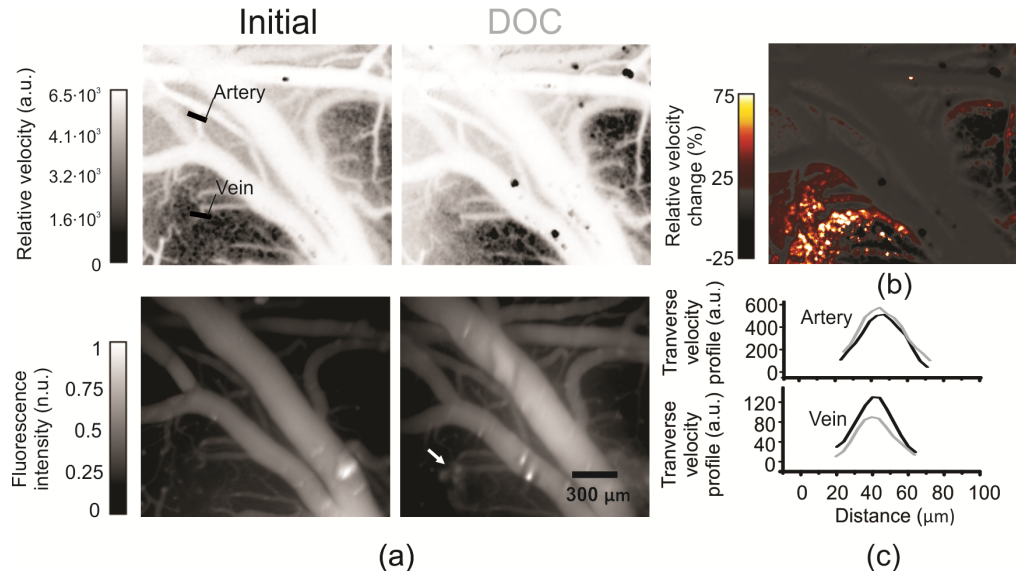

Fig. 9. Small permeability changes in vessels due to DOC application to a live rat brain. (a) Fluorescence intensity and blood flow relative velocity maps before and after DOC application. In some discrete locations, an accumulation of fluorescent dye is observed in the extravascular region (white arrow). There is a slight change in the blood velocity map (top), correlated with the observed small changes in intensity outside the vessels in the fluorescence map (bottom) (b) Relative changes of velocity after DOC application. (c) Transverse relative blood velocity profiles for an artery (upper) and a vein (bottom) before and after DOC application. Initial profiles blood velocity profiles (black) and the final blood velocity profiles (grey) after DOC application are overlaid in the figure. Spatial Locations of the plotted profiles are highlighted in black in *(a)*, top left panel.

Table 1. Measured and simulated velocity values for the vessels marked by a number in Fig. 11. Velocities were measured with the time of flight technique under green LED illumination along the lines highlighted in Fig. 11. Given the challenges in translating the vessel morphology accurately into COMSOL, the simulations did not converge for a portion of the vessels.

Segment	Measured	Simulated	Absolute Variance [%]
1	0.371	–	–
2	0.457	–	–
3	**1.503**	**1.690**	**12.4**
4	**0.563**	**0.454**	**19.4**
5	0.605	–	–
6	**0.167**	**0.141**	**15.6**
7	**0.932**	**0.697**	**25.2**
8	**0.374**	**0.332**	**11.1**
9	**0.247**	**0.253**	**2.4**
10	**0.371**	**0.348**	**6.2**
11	0.4	–	–
12	0.175	–	–
13	**0.282**	**0.278**	**1.4**
14	**0.261**	**0.251**	**3.8**
15	0.262	–	–
16	0.311	–	–
17	0.254	–	–
18	0.475	–	–
19	0.437	–	–
20	0.389	–	–
21	0.476	–	–
22	4.162	–	–
23	–	–	–
24	0.138	–	–
25	**0.369**	**0.358**	**3.0**
26	0.574	–	–
27	2.608	–	–
28	**1.157**	**1.440**	**24.5**
29	**0.961**	**0.713**	**25.8**
30	**0.643**	**0.662**	**3.0**
31	0.125	–	–
32	0.571	–	–
		Mean	**12.0**
		Stdev	**9.0**

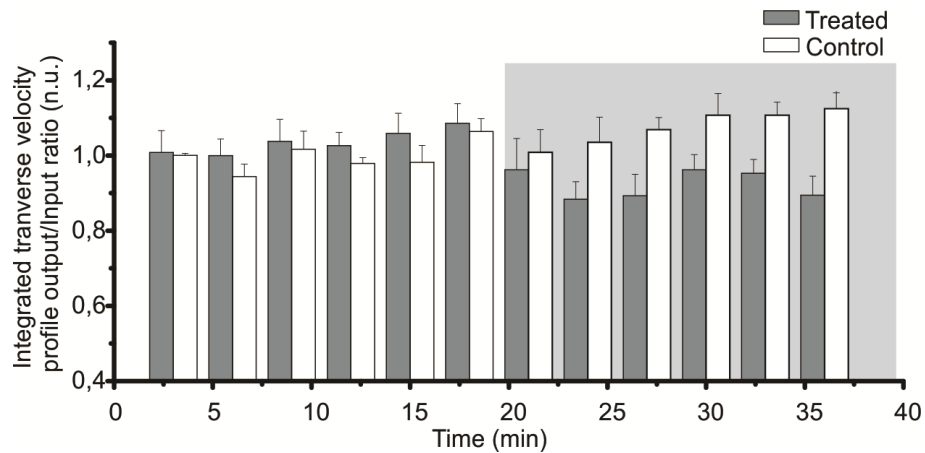Fig. 10. Time course of the normalized integrated transverse output/input profile ratio (N = 2 rats, data shown as mean ± SE). Grey bars represent the treated hemisphere and white bars the untreated hemisphere. DOC application period is marked with a grey box.
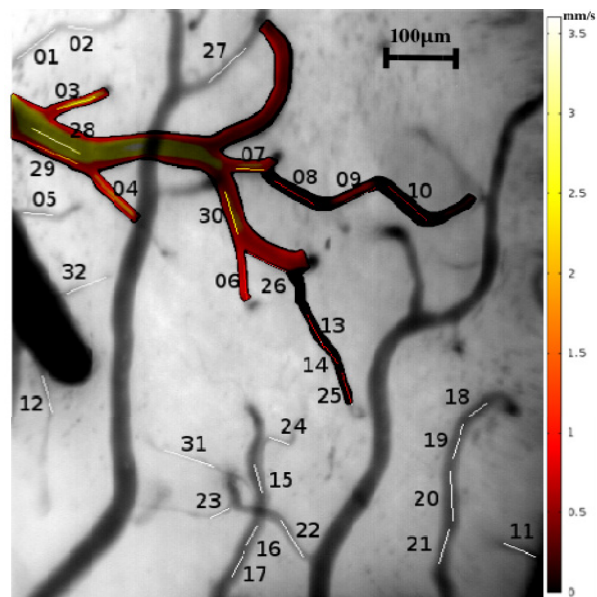

Fig. 11. Overlay of simulated (colored map) and measured vessel morphology maps (grey level map). The color-coded velocities are in [mm/sec].
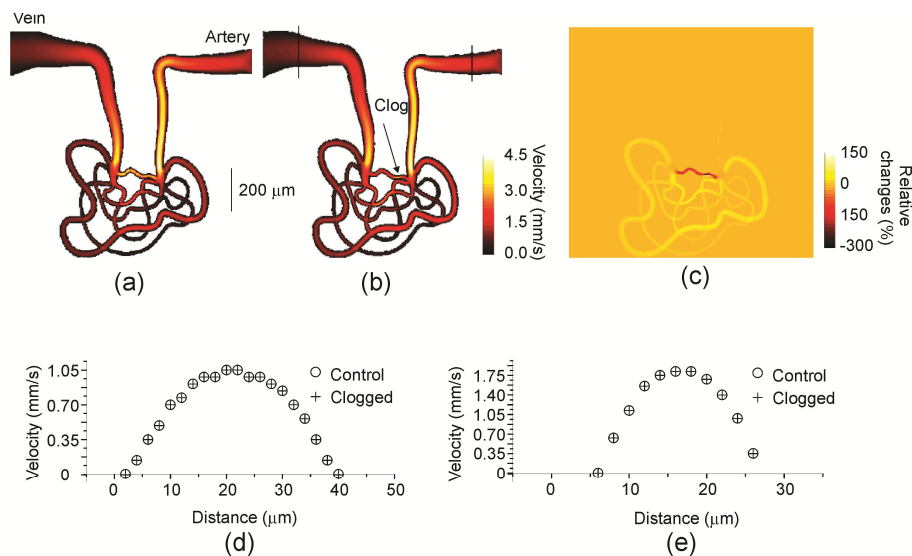
Fig. 12. Simulated effects of a localized clog on velocity maps. a-b) Velocity maps without (a) and with (b) an occlusion. The arrow in (b) shows the location of the clogged zone (smaller diameter over a length of 20 µm). (c) Velocity changes calculated as $100*((v_f - v_i)/v_i)$ where v_f is the final velocity (with an occlusion) and v_i stands for the initial velocity. (d) Initial (black dots) and final (grey cross) transverse velocity profile of a simulated vein. (e) Initial and final transverse velocity profiles of the simulated artery. Lines along which the profiles were taken are marked in panel (b).

Acknowledgments